Journal of Materials Processing Tech. 314 (2023) 117888

Contents lists available at ScienceDirect

Journal of Materials Processing Tech.

journal homepage: www.elsevier.com/locate/jmatprotec

Electromagnetic field-assisted laser welding of NiTi to stainless steel: Towards a lightweight, high-strength joint with preserved properties

Behzad Farhang [a], Ahmet Alptug Tanrikulu [b], Aditya Ganesh-Ram [a], Ankur Jain [a], Amirhesam Amerinatanzi [a,b,*]

[a] Mechanical and Aerospace Engineering, University of Texas at Arlington, Arlington, TX, USA
[b] Materials Science and Engineering, University of Texas at Arlington, Arlington, TX, USA

ARTICLE INFO

Associate Editor: Hui-Ping Wang

Keywords:
Dissimilar laser welding
Shape memory alloys
Magnetic field
Intermetallic component
Transformation temperature
Mechanical properties

ABSTRACT

In recent years, laser welding has attracted significant attention as a promising technology for joining smart alloys (e.g., NiTi) to structural materials (e.g., SS) thanks to its unique advantages such as exceptional control heat input and narrow fusion zone. However, obtaining a high strength weldment that also preserves the functional properties of the materials being joined together remains a key challenge in this field mainly due to the formation of brittle intermetallic components (IMCs) near and at the interfacial zone. This study investigates a novel technique for laser welding processing of NiTi/SS assisted by an external magnetic field. This technique, referred to as magnetic field supported, is hypothesized to suppress the formation of brittle intermetallics (e.g., TiFe and $TiFe_2$) during the laser welding of NiTi/SS, which, in turn, may improve the performance of the resultant joint. To test the hypothesis, comprehensive experimental assessment of the evolution of structural, mechanical and thermomechanical properties of NiTi/SS joints has been conducted. The findings demonstrate the full suppression of Ti-Fe-based IMCs in the joint area, accompanied by significant improvement in the strength (by 28 %) and ductility (by 137 %) of the MFSed joint when compared with conventional laser welding. Interestingly, negligible changes (~0.6 °C) in the martensitic transformation temperatures have been obtained.

1. Introduction

The remarkable properties of shape memory alloys (SMAs) have facilitated their applications in the aerospace industry (Hartl and Lagoudas, 2007), sealing connections in hydraulic systems (Quan and Hai, 2015), oil drilling and bearing applications (DellaCorte, 2017), biomedical implants (Patel et al., 2020), and automotive industry (Sadashiva et al., 2021). Nickel-Titanium (NiTi), as the most commonly used SMAs (Elahinia, 2016), offers unique shape memory effect (SME) and superelasticity (SE) behavior (Oliveira et al., 2016). One of the main challenges that hinder the extensive use of NiTi in the aforementioned industries arises from difficulties associated with the joining of NiTi SMAs to other structural components (e.g., stainless steel) of a larger assembly (Li et al., 2013). This issue is of particular importance , because NiTi SMAs standalone do not offer required strength in critical applications, not to mention the other advantages that would be accompanied when bimetals are used. As an example, in the upcoming Mars Rover mission, and more specifically for its wheel assembly, NiTi wires that are capable of withstanding high level of deformation (up to 8 %) are needed to be connected to a wheel rim which is made of a high strength, machinable, structural material, while preserving the lightness of the joint (Ellery, 2016).

Laser welding technology has been reported to be one of the most effective techniques (Zeng et al., 2017) in joining NiTi SMAs to SS structural materials due to its unique advantages such as lightweight joint, contrability on process parameters, and significant reduction in the width of fusion zone (FZ) and heat affected zone (HAZ) (Mehrpouya et al., 2019). However, this technique has been found to be associated with a considerable reduction in the NiTi/SS joint mechanical properties (Falvo et al., 2005), a significant change in the martensitic transformation temperatures, and a consequent deterioration in the functionality (i.e., SME and SE) of NiTi material (Chan et al., 2011). The main reason for the deterioration of mechanical properties and functionality in the FZ and HAZ of NiTi/SS joint is the microstructural evolution and more specifically the formation of brittle IMCs (Li et al., 2013). Generally speaking, similar behavior has been reported in

* Corresponding author at: Mechanical and Aerospace Engineering, University of Texas at Arlington, Arlington, TX, USA.
E-mail address: amir.ameri@uta.edu (A. Amerinatanzi).

https://doi.org/10.1016/j.jmatprotec.2023.117888
Received 29 August 2022; Received in revised form 9 January 2023; Accepted 21 January 2023
Available online 23 January 2023
0924-0136/

welding of wide range of dissimilar material together because of formation of brittle IMCs (Bhanu et al., 2022).

Up to now, several novel approaches have been proposed to prevent the formation of brittle IMCs in dissimilar laser welding of NiTi. Some studies demonstrated that a proper selection of laser welding process parameters (i.e., laser power, scanning speed, laser focus diameter and etc.) can relatively affect the diffusion of elements in the FZ and hence reduce the brittle IMCs to some extent. The technique has shown slight increase in the strength of the NiTi/SS joint (Gugel et al., 2008). Using an interlayer to prevent direct diffusion of SS and NiTi elements into each other and consequent reactions is the most common technique in dissimilar laser welding of NiTi. Li et al. used Co (Li et al., 2013) and Ni (Li et al., 2012) interlayers in joining NiTi to SS and reported ultimate strength of 347 and 372 MPa, respectively, for the NiTI/SS joint. Shamsolhodaei et al. used an Ni interlayer and observed an increase in the tensile strength, from around 200–410 MPa (Shamsolhodaei et al., 2020). Although addition of an Ni interlayer prevented diffusion of SS elements toward NiTi side, it made the joint heavier and also induced IMCs (i.e. Fe_3Ni) formation. Moreover, this interlayer addition affected the martensitic transformation temperatures because of its reaction with SS and NiTi. More recent proposed technique in laser welding of NiTi/SS joint was laser offset welding technique where the laser beam was offset toward the SS side relative to the interface of two dissimilar metals (Shamsolhodaei et al., 2020). This technique was the only reported study which effectively led to a reduction in formation of IMCs in dissimilar joining of SMAs and resulted in a lightness of the joint. Although the results of tensile strength have shown improvements (up to 410 MPa), still some brittle compounds have been observed in the FZ. To overcome this challenge, Zhang et al. combined the laser offset welding with interlayer technique (Cu interlayer) and reported a NiTi/SS joint with no sign of brittle IMCs. Due to the low achieved ultimate strength in the joint (~153 MPa), as it is obvious, the requirement of lightness was not satisfied (Zhang et al., 2020).

While not tested in the field of laser welding of SMAs, and more specifically suppression of brittle IMCs, several studies have been reported in the literature to use a magnetic field (MF) to control the diffusion of elements during laser welding as a way to exert an upward electromagnetic force. It has been shown that such MF can slow down or prevent the downward movement of SS hot element during laser welding of stainless-steel sheets (which leads to keyhole stabilization). Such addition led to improvement in the welding quality as well as ultimate strength of the joint (Chen, 2020). Moreover, a number of studies investigated the effect of MF in dissimilar laser welding on different aspects of laser welding such as the melt flow, weld geometry and microstructure evolution (Huang et al., 2020).

Such capability of MF in controlling diffusion of element motivated authors to control the diffusion of SS elements toward NiTi side, for the first time, by a novel configuration of MF during a dissimilar offset laser welding of these two materials. The MF was engineered in a way to result in a so-called braking Lorentz force toward the SS side (instead of upward force in literature) which hinders their movements toward NiTi material. Then, this study focuses on the effect of the proposed technique in reducing the formation of IMCs in the FZ and HAZ of laser welded NiTi/SS joint. To investigate this in detail, scanning electron microscopy (SEM), energy-dispersive X-ray spectroscopy (EDS) and X-ray diffraction (XRD) analysis have been conducted to trace the structural evolution (grain morphology as well as chemical composition) in HAZ and FZ. Then, the consequent changes in the material properties (strength and transformation temperatures) due to the presence of the MF are investigated through experimental mechanical tensile, hardness tests as well as differential scanning calorimetry (DSC) tests.

2. Materials and methods

2.1. Materials

Round wires of 0.8 mm diameter-a superelastic NiTi alloy provided by Nexmetal Corporation (Sheridan, WY, USA) and a SS wire procured from Master of Clouds (Beavercreek, OH, USA) - were selected for the laser welding experiments. The NiTi alloy used in this case was austenitic at room temperature and, therefore, superplastic. The composition of the base materials (BMs) is presented in Table 1. The ends of wires were surface grinded to maintain better contact between the mating surfaces of the wires before laser welding. The wires were cleaned using isopropyl alcohol to remove any possible surface impurities.

2.2. Laser welding

As shown in Fig. 1, laser welding was performed in two different situations: (i) non-magnetic field supported (nMFS) and (ii) magnetic field supported (MFS) laser welding. In both cases, the laser beam was focused at a 200 μm offset distance from the interface toward the SS BM.

An iWeld 990 series 60-Watt benchtop laser welding machine by LaserStar Technologies (Riverside, RI, USA) was used for butt welding the wires. The source of the laser was Nd:YAG with a peak power of 60 Watts. All the laser welds were made using a single pulse top hat profile with a spot diameter of 0.8 mm and a pulse duration of 30 ms. Throughout the welding, Argon shielding gas was supplied at 0.34 m^3/h, starting from at least 30 s prior to welding in order to prevent oxidation over the FZ. The wires were clamped together in order to stabilize the joint and achieve better weld quality.

In the MFS laser welding, a set of two Neodymium permanent magnets of size 19 × 12.7 × 6.35 mm^3 was mounted above (South pole) and below (North pole) the weldment (Fig. 1b). These magnets were orientated such that their widest faces formed North and South poles. Per classical definition of magnetic force, the Lorentz force (F_L) can be calculated through $\vec{F_L} = q\vec{V} \times \vec{B}$ equation. where q, $\vec{V}$ and $\vec{B}$ are moving charge, the velocity vector and the magnetic field vector, respectively. Here the $\vec{F_L}$ was preferably engineered to be along the wires toward the SS side (i.e., producing a Lorentz braking force that prevents free diffusion of SS to NiTi side). The direction of the velocity vector can be extracted from the direction of the self-induced thermoelectric currents (resultant of Seebeck effect) calculated in simulation literatures on the laser welding of stainless steel. From Chen *et. al* (Chen et al., 2018), this negative moving charge has a velocity direction of 60-degree downward with respect to the plane include the laser direction and material axis. Then, based on the aforementioned formula, the B direction should be oriented by a 30-degree orientation with respect to the wire axis. The resultant axis of magnets was then orientated to have a 30-degree tilt upward to the vertical axis as viewed from a cross section (Fig. 1c). The vertical distance between the top surface of the magnet and the lower surface of the weldment was set to 30 mm to adjust the magnetic flux density in the molten pool. During MFS laser welding, the laser beam and magnet remained static to deliver a uniform magnetic flux density in the molten pool throughout the welding process. The experimental set-up is shown in Fig. 2.

2.3. Experiment method

A Bruker D8 Advance X-ray diffractometer (Bruker Corporation, Madison, WI, USA) was used to perform the compositional analysis of FZ and HAZs. The Cu k-alpha X-ray source had a wavelength of 1.5406 Å, current of 40 mA and voltage of 40 kV. Measurements were taken at room temperature with step interval and scan speed of 0.04° and 1 s/step, respectively, as the 2θ varied between 30° and 100°. The WZ (including both HAZs and FZ) of eight parallel weldments was scanned

Table 1
Manufacturer-provided properties of the two BMs used.

Material	Wire Composition (wt %)										Austenite finish temperature - A_f
	Ni	Ti	Cr	Mn	Mo	Si	C	P	S	Fe	(°C)
NiTi	71.4	28.6	-	-	-	-	-	-	-	-	-10
SS 316 L	21.2	-	9.78	0.79	2.05	0.42	4.88	≤ 0.04	≤ 0.03	Bal.	-

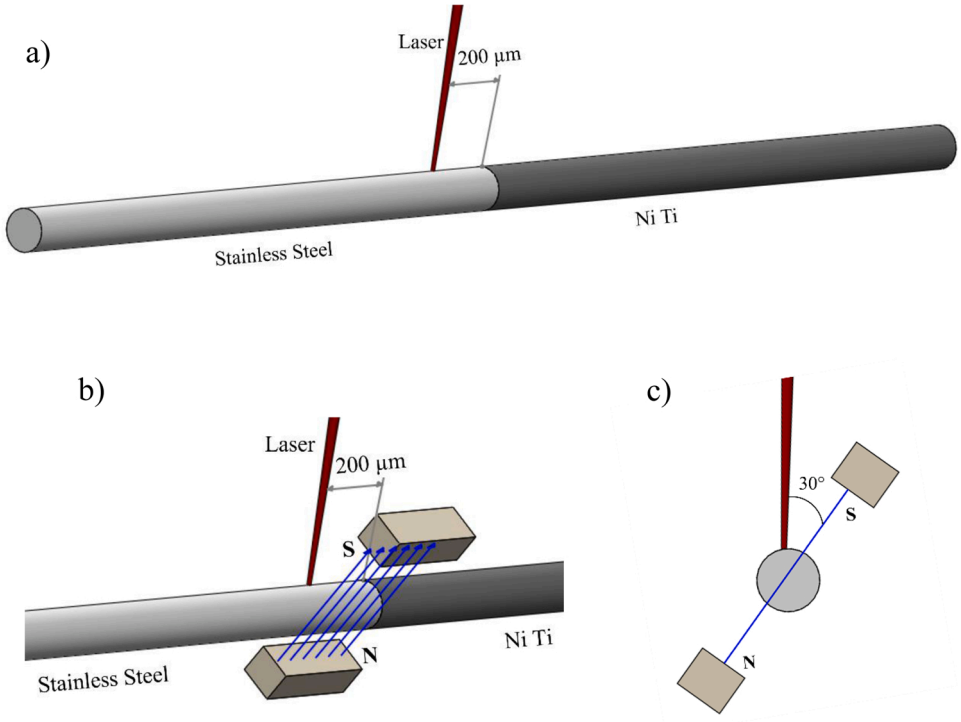

Fig. 1. a) nMFS welding arrangement, b) MFS welding arrangement and c) MFS welding arrangement side view.

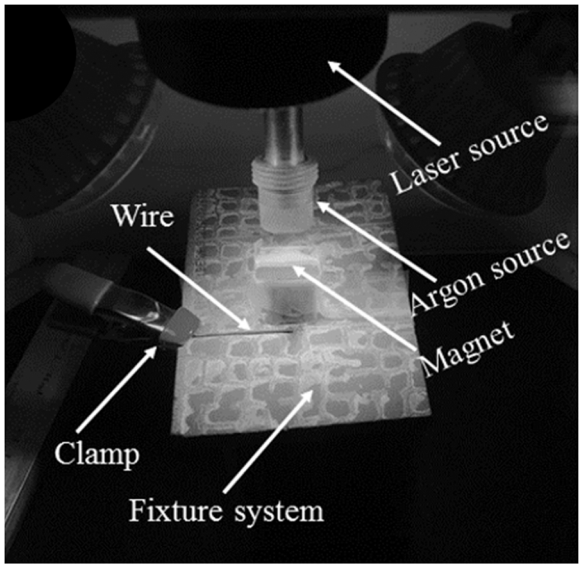

Fig. 2. Experimental set-up used for laser welding.

for each case to obtain an appropriate sample size for XRD analysis, as was done in a similar study (Mirshekari et al., 2013). The X'Pert High-Score Plus software, equipped with ICDD PDF-2 databases, was used to analyze the XRD diffractograms.

In order to perform the metallographic analysis, the weldments were incorporated into a polymeric resin. To study the weld region along its depth, the welded wires were loaded such that the thickness through which the laser penetrated the wires was parallel to the flat surfaces of the epoxy. The mounted samples were then polished using an E-prep 4TM polisher (Allied High-Tech Products Inc., Rancho Dominguez, CA, USA) with progressively finer grained Silicon Carbide (SIC) papers. Polishing was performed using a DiaMat polishing cloth with 1 µm diamond suspension, followed by polishing the surface of the sample on a Red Final C polishing pad using 0.04 µm colloidal silica suspension. The NiTi wire was etched using Kroll's Reagent (1–3 mL HF, 2–6 mL HNO_3, 100 mL water) (ES Laboratory LLC, Glendora, CA, USA), and oxalic acid (10 g oxalic acid, 100 mL water) (ES Laboratory LLC, Glendora, CA, USA) was used as an etchant for the SS side. Samples were cleaned by alcohol and compressed air prior to microstructure tests.

A Hitachi S-3000 N variable pressure scanning electron microscope (Hitachi, Santa Clara, CA, USA) was used for microstructure characterization. This instrument provides a resolution of 3.5 nm for the secondary electron images using a tungsten electron source. The same electron microscope, equipped with a 15 mm working distance Oxford Inca energy-dispersive X-ray spectroscopy (EDS) detector was employed to evaluate the variation of chemical elements throughout the BM, HAZ and FZ. The EDS utilizes a light element Si (Li) X-ray detector. The Vickers hardness measurements were performed with a LECO LM 300 AT Micro Hardness Tester (LECO, St. Joseph, MI, USA). The indentation was performed with 1 kg force applied for 10 s based on ASTM E92 standard. 19 indentations were made along the length of the wire such that the indentations cover both BMs along with the weld region. An

average of at least 3 indentations were used to calculate the hardness of each point.

Tensile testing was carried out by a 100 kN Shimadzu EHF E-series tensile tester handled by a 4830-servo controller. Four Aluminum plates with dimensions of 40 × 35 mm^2 were designed to ensure better gripping of wires during testing. The weldments were held tightly within two plates on either side of the gripper within grooves machined with 0.8 mm width and 0.38 mm depth on each plate. The design was developed such that the two plates would hold their respective wires tightly after being placed in the grips. The test speed was set at 0.25 mm/min for both nMFS and MFS samples.

To analyze the transformation temperatures of the NiTi BM and welded specimens, a TA Instruments Q20 Differential Scanning Calorimeter (TA Inc., New Castle, DE, USA) equipped with a refrigerated cooling unit was used. Differential Scanning Calorimetry (DSC) tests were performed at temperatures ranging from −50 to 110 °C and the heating/cooling rate was set at 5 °C/min. A region on the NiTi side, very close to the FZ, was cut from the weldments for the DSC analysis. DSC samples were cut out from the NiTi side of the weldments. An approximate location from which the samples were cut out is shown in Fig. 3. Dashed line regions show the location of the cubic samples on the NiTi BM side, each sample has 0.5 × 0.5 × 0.5 mm^3 cubic geometry.

3. Results

3.1. Microstructural analysis

Scanning electron microscopy (SEM) images for the nMFS and MFS samples are presented in Fig. 3. While larger and more numerous defects can be observed for the nMFS sample, a few small pores were also found in the MFS sample at the center of FZ. The width of the WZ decreased under the effect of the magnetic field. According to the EDS analysis (presented in the next section), around a 100 μm reduction in the average width of FZ for the MFS sample as compared to the nMFS sample was noted. Moreover, while the average width of HAZ for the SS side remained unchanged under the effect of the magnetic field, the average width of HAZ toward the NiTi side decreased dramatically to around two-thirds of the nMFS sample. The average width of FZ and HAZ is reported in Table 2 for both samples.

Fig. 4 shows the SEM micrographs in the weld interfaces of SS and NiTi for both nMFS and MFS samples. A structural grain transformation was observed from the center of the FZ toward HAZs for both cases. For the nMFS sample, relatively large equiaxed grains formed at the center of the FZ and moving toward the SS, it was changed to columnar and then planar (Fig. 4a). Columnar grains were seen to elongate towards the BM. From Fig. 4c we can see that toward the NiTi side, the equiaxed grain structure formed at the center of FZ was changed to columnar and then cellular for this sample. Columnar grain growth on the NiTi side of the FZ (Kumar et al., 2021) shown in Fig. 4 is the source of the elemental diffusion a cross the FZ to HAZ interface. As a result of inter-dendritic segregation (Kumar and Pandey, 2022a) during the columnar growth compositional variation of the Cr and Ni alloying elements shown in Fig. 5. The SEM results revealed the orientation of columnar grains to be aligned parallel to the cooling direction. As can be seen, a reaction layer zone (RLZ) was formed in the NiTi HAZ. This multi-structure layer placed a high number of precipitates and IMCs for the nMFS sample. Similarly, for the MFS sample, small equiaxed grains were formed at the center of FZ, with finer grains being formed in this sample.

Table 2
Dimensional analysis of FZ and HAZs for nMFS and MFS samples.

Sample	Average width of FZ (μm)	Average width of NiTi-HAZ (μm)	Average width of SS-HAZ (μm)
nMFS	651 ± 20.3	29.6 ± 4.6	45.2 ± 7.2
MFS	547.4 ± 19.8	14.8 ± 3.5	44.4 ± 6.9

The same grain structure transformation was also observed for MFS sample. From the FZ to HAZs, the structure was changed to columnar and then planar toward the SS side (Fig. 4b). Like the nMFS sample, the columnar grains formed toward the SS in terms of orientation. When it comes to the NiTi side, structure of grains changed to columnar and then cellular moving toward the BM (Fig. 4d). Unlike the nMFS sample, a random orientation was observed for the columnar grains formed in this zone. The RLZ formed in the MFS sample was found to be narrower when compared with the nMFS sample, with no sign of precipitation and formation of IMCs being observed in this zone.

The effect of the magnetic field on electron movement has changed the heat transfer rate which was carried by the electrons during the solidification and growth. Consequently, a variation of the solidification phenomenon was observed between nMFS and MFS applications. Deviation of the electron movements from the FZ – NiTi BM interface decreases the total number of the electrons at that region, hence the total heat decreases. Additionally, magnetic field has effect on melt motions (Chen et al., 2018) which effects the heat dissipation. In MFS application lesser heat input and promoted melt motions cause a faster cooling rate which is resulted with narrower HAZ region (Fig. 4).

Heating the NiTi BM causes deviation from the initial microstructure which is shown in HAZ for both nMFS and MFS in Fig. 4a) and b) respectively. Higher heat inputs distribute lower cooling rates in nMFS which resulted with wider HAZ. Consequence of heat input variance in nMFS application, Fig. 5 shows that at % of Ni is lower in HAZ compared to MFS. Chemical composition and microstructural change during of nMFS welding ended with major reduction of the TT.

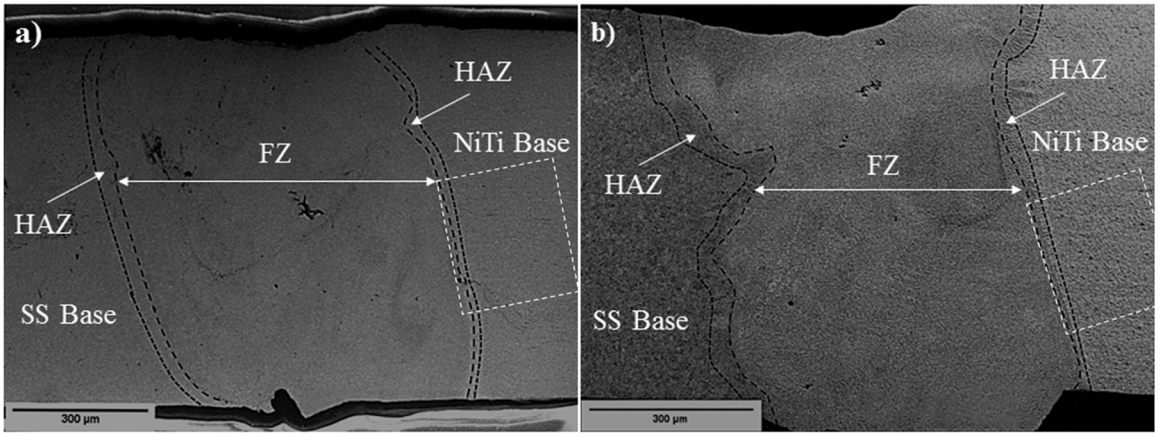

Fig. 3. Comparison of cross-sections of the WZ for the a) nMFS and (b) MFS samples.

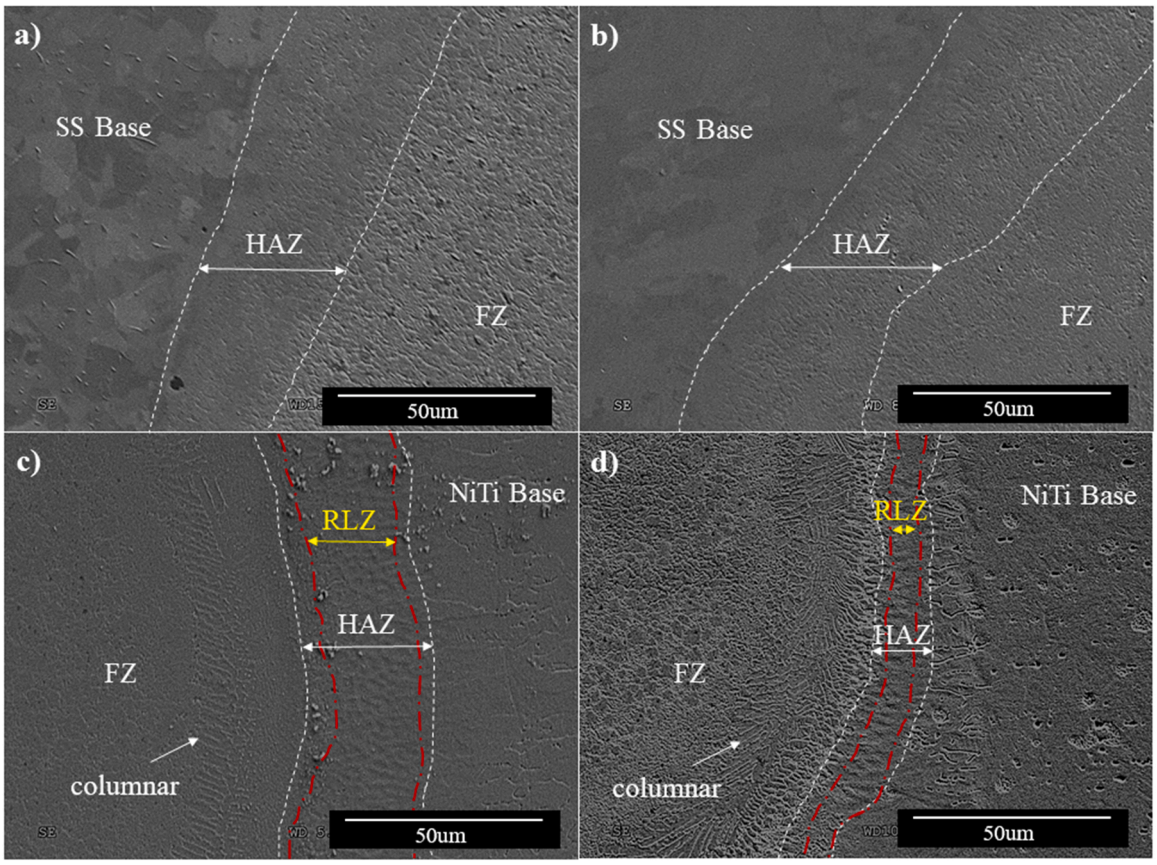

Fig. 4. Microstructure of weldments at weld interface of: (a) SS for nMFS sample, b) SS for MFS sample; and at weld interface of:(c) NiTi for nMFS sample and (d) NiTi for MFS sample.

3.2. EDS analysis

The effect of a magnetic field on the chemical composition of the welded joint was studied using EDS analysis. Fig. 5 shows the variation in the distribution of Titanium, Nickel, Iron and Chromium for both nMFS and MFS samples. The average width of the FZ and HAZ can be extracted by determining the points at which a sudden change occurred in the level of atomic percentage of elements. These zones were shown on EDS plots as their variation between samples discussed in previous section. Comparison of variation of two main elements (Fe and Ni) showed higher fluctuation for the nMFS sample, with around 35 % and 30 % (for Fe and Ni respectively) lower fluctuation being observed in the MFS sample. Reduction of Titanium in the FZ due to the application of a magnetic field can be observed by comparing the atomic percentage in Fig. 5a and b. Similarly, by implementing a magnetic field, the Nickel distribution in the weld metal has also been decreased as can be seen in Fig. 5b.

For an accurate analysis of variation of elements at the FZ, the root mean square (RMS) value was calculated and reported in Table 3 for both nMFS and MFS samples. Comparing the samples, higher atomic percentage of Fe and Cr was found in the nMFS sample (more than 9 % and roughly 24 % respectively), which shows higher contribution of SS in formation of the FZ for this sample. By contrast, around 8.5 % and 12.5 % reduction in atomic percentage of Ni and Ti were respectively observed under influence of the magnetic field.

3.3. X-ray diffraction (XRD) analysis

Fig. 6 provides the XRD patterns of the WZ in both nMFS and MFS samples. As observed from the patterns, the main phase for both samples was detected as austenitic B2 phase. While the γ-Fe parent phase was observed for both samples, the ferrite α-Fe was detected only in nMFS sample. The IMCs detected by XRD are in agreement with a previous study which reported similar phases for the laser welding of NiTi to SS (Mirshekari et al., 2013).

As can be seen, several extra peaks were detected for the nMFS sample demonstrating the higher probability of formation of IMCs. In the case of common NiTi precipitates, more peaks associated with the formation of Ti_2Ni were observed in the nMFS sample. Also, the formation of Ni_3Ti was observed for both samples with one more peak being detected for the nMFS sample. When it comes to the IMCs formed due to the combination of dissimilar materials, precipitations of FeNi and $TiCr_2$ were found probable for both samples. However, a higher number of peaks related to these phases were found for the nMFS sample. In the case of main brittle phases, a major difference became evident between samples. While formation of both TiFe and $TiFe_2$ phases was detected for nMFS sample, there was no sign of precipitation of these IMCs in the MFS sample.

3.4. Microhardness

The Vickers microhardness values have been obtained across the WZ in both samples which are then plotted in Fig. 7. According to the measurements, a decreasing trend in hardness was observed from the WZ to the BMs for both nMFS and MFS samples. Starting from the BMs, an upward trend observed toward the HAZ followed by a sudden drop in value which again rises to the peak occurring at the center of the FZ. This similar variation and trend have been reported by previous studies for the laser welding of NiTi to SS (Li et al., 2013). Overall, in the nMFS sample, a higher average hardness value was found for the areas close to the WZ. Moreover, the difference between the hardness value of the WZ and BMs was less. In this case, the highest microhardness value (658 HV)

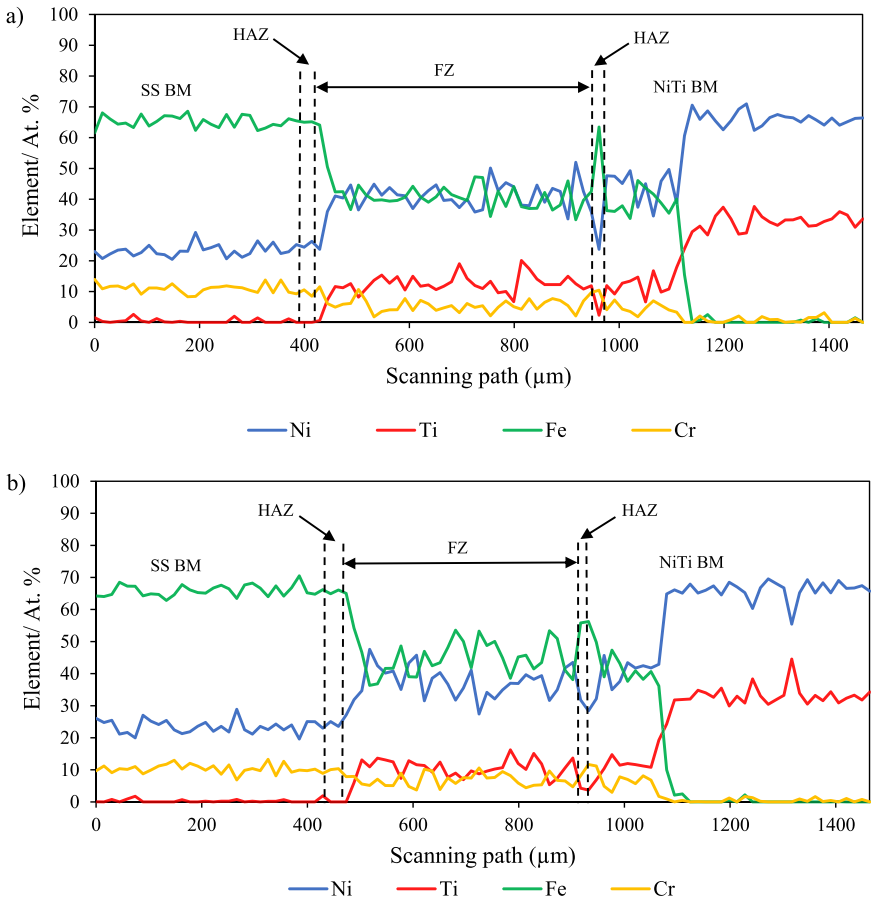

Fig. 5. Distribution variation of Ni, Ti, Fe and Cr in weld region for a) nMFS and b) MFS samples.

Table 3
RMS atomic percentage composition of elements in FZ for both nMFS and MFS samples.

Element	*nMFS*	*MFS*
Ni	*41.78*	*38.26*
Ti	*12.78*	*11.19*
Fe	*41.02*	*44.86*
Cr	*5.79*	*7.17*

appears to be in the center of the FZ. In the case of MFS sample, the highest microhardness value (409 HV) was found at the same location. It should be noted that the difference between the hardness value of the WZ and BM was less for the MFS sample.

3.5. Mechanical testing results

Characteristic stress–strain curves from tensile testing for the BMs as well as nMFS and MFS samples are shown in Fig. 8. For the nMFS sample, the wire was deformed plastically and finally fracture occurred at the stress level of 338 MPa and strain of 0.56 %. The rupture stress obtained for this joint was about 21 % of the level measured for the NiTi BM and 48 % for the SS BM. In terms of strain, elongation at break was observed at 3.4 % of that of NiTi BM and 1.37 % of that of SS BM. In the MFS sample, a noticeable improvement can be seen in both tensile strength as well as ductility. The MFS sample showed an ultimate tensile strength of 431 MPa and strain of 1.33 %, which is respectively 28 % and 137.5 % higher than that of nMFS sample. The rupture stress observed for this sample is equivalent to 27 % of NiTi BM and 61 % of SS BM. Also, the elongation for this sample was found equivalent to 8.16 % of NiTi BM and 3.24 % of SS BM.

It was observed that ductility of the welded joint is lower than the BMs which is a result of the chemical composition difference and microstructural variance of the FZ and BM. Fig.4 shows the microstructure transition from FZ center towards the NiTi BM interface.

Fracture surface of the wires after tensile test evaluated under SEM. Shaded areas in Fig. 9 shows the ductile deformation regions of the nMFS and MFS welding application. In both applications fracture occurred in NiTi – FZ interface and images in Fig. 9 delivers the surface of the NiTi wire side of the interface. It was observed that ductile deformation region in MFS application is greater than nMFS application. Deformation during the tensile test listed as % elongation for multiple applications in Table 4.

3.6. DSC

Fig. 10 depicts the DSC measurement of the transformation temperatures of the NiTi for the BM and weldments. The austenitic (B2), martensitic (B19′), and R phase were determined using the peaks identified on the plots. In most of the cases, the transformation between austenitic and martensitic phases occurred through formation of R phase. To compare the transformation temperature between the samples, austenite finish temperature (A_f) was selected and extracted from the plots. According to the results, the A_f was identified as 24.7 °C for the NiTi BM. Analyzing the data showed around 20 °C reduction in A_f for the nMFS sample, with the A_f being identified as 4.9 °C for this sample. However, the MFS sample maintained the transformation temperatures observed for the NiTi BM. The A_f was found 24.1 °C for MFS sample with its profile resembling the one extracted for the NiTi BM.

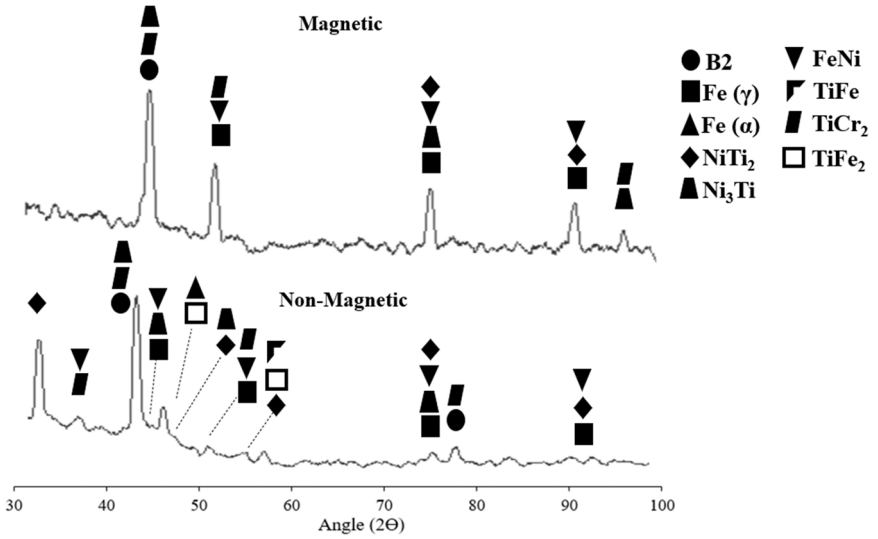

Fig. 6. XRD patterns extracted from WZ of NiTi-SS for nMFS and MFS samples.

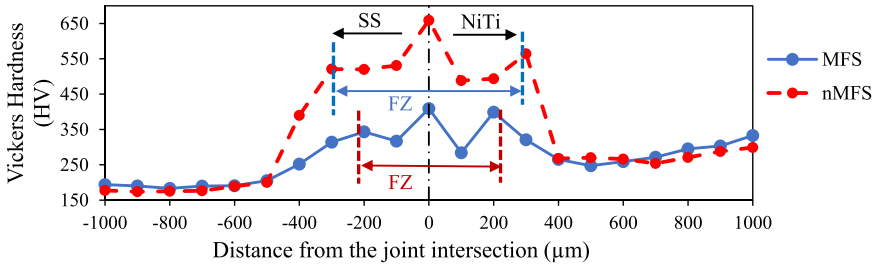

Fig. 7. Microhardness profile for NiTi-SS non-magnetic and magnetic welding.

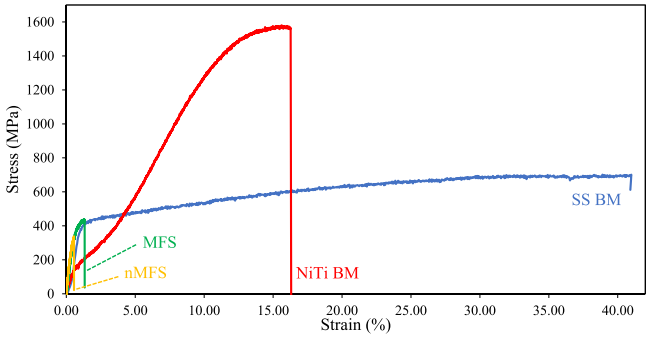

Fig. 8. Stress-strain plots for the nMFS and MFS samples, and BMs.

4. Discussion

In terms of microstructure, the cross section of the WZ for both weldments was revealed and analyzed using SEM results. According to the SEM micrographs (Fig. 3), the HAZ observed for the weldments was shorter on the NiTi side for both samples. (Möller and Thomy, 2013) reported the same observation for the offset welding of dissimilar materials. In this case, the laser focus offset implemented on the SS side can restrict the melt pool from wetting a larger region of the NiTi side to preserve it from intense heating exposure.

When it comes to the formation of the melt pool during the welding process, a large notch was observed at the bottom of the melt pool for the nMFS sample, indicating the formation of a shallower pool. In contrast, a full penetration of molten material, which resulted in a deeper melt pool and a defect free weld, was observed in the MFS sample. (He et al., 2018) reported the formation of defects and porosity in the melt pool as a common and critical problem in laser welding which leads to a reduction in the effective area subjected under loading and causes stress concentration, solidification cracking, and deterioration of mechanical properties. (Vollertsen and Thomy, 2006) attributed the lower levels of defects during the MFS laser welding to the stirring effect and less stress concentration arising from the effect of Lorentz force. (Zhou et al., 2021) investigated the effect of static magnetic field on laser welding of Magnesium/Aluminum plates. They observed an increase in Reynolds number and magnitude of vorticity under the influence of magnetic field which results in a rotary motion of the molten material in melt pool (stirring effect). This stirring effect arises from the Lorentz force which accelerates the flow rate of the molten material, enlarges the flow region of the molten metal around heat source and thereby improves the keyhole mode. This leads to the formation of a deeper pool which is proven to improve the heat efficiency of the welding pool and reduce the temperature gradient which therefore promotes the mass transfer and cooling rate in the melt pool. In this case, (Zhou et al., 2021) achieved a better weld quality (formation of less brittle IMCs) with lower level of defects under the influence of a magnetic field. This explains less formation of pores and cracks for the welding performed under the support of a magnetic field. Moreover, (Cao et al., 2020) observed lower level of defects in laser welding of Aluminum alloy plates under a permanent magnetic field because of a reduction in the stress concentration. This also aligns with the lower level of defects observed in this study for the MFS sample compared to nMFS weldment.

Morphology of grains was also revealed using SEM results generated for the WZ of both samples. While similar grain structure was found for both nMFs and MFS weldments toward the SS side, the magnetic field influenced the formation and orientation of grains on the NiTi side. In

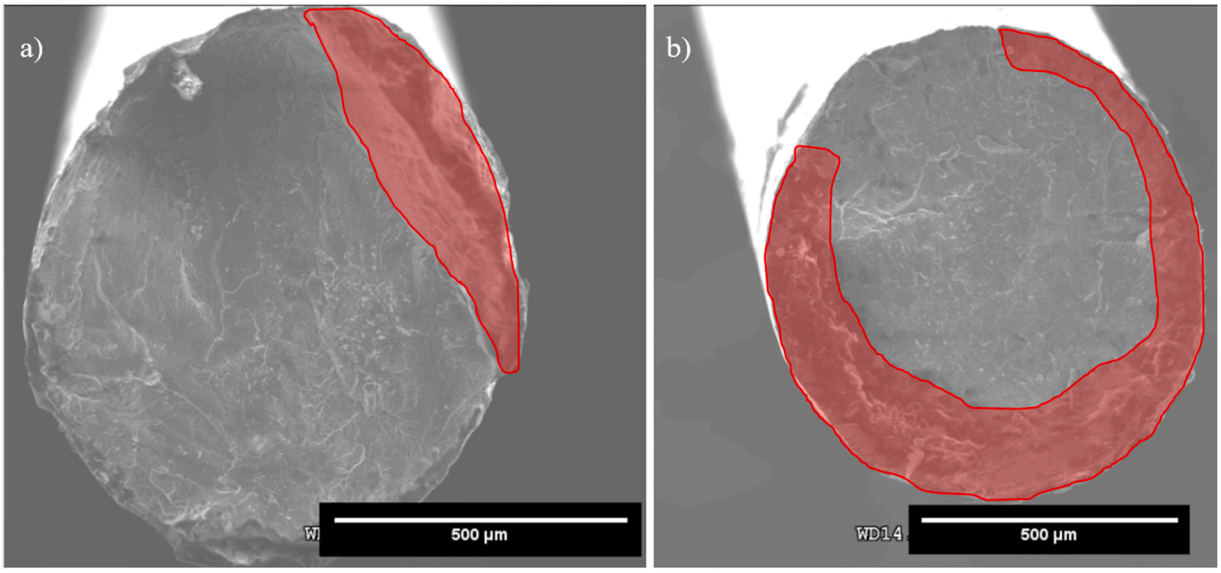

Fig. 9. Ductile deformation regions of the fracture surface: a) nMFS b) MFS.

Table 4
Tensile Tests for nMFS and MFS application with fracture locations.

Sample	UTS (MPa)	Elongation (%)	Fracture Location
nMFS	347.08 ± 16.35	1.115 ± 0.165	NiTi - FZ Interface
MFS	426.07 ± 10.86	0.689 ± 0.22	NiTi - FZ Interface

terms of structure, a transformation from equiaxed to columnar and then planar can be seen for both samples from the center of the FZ toward the SS HAZ (Fig. 7a and b). This can be attributed to the constitutional supercooling (CS) which occurs during solidification. Phenomenon of CS which occurs at the solid/liquid interface during the solidification depends on temperature gradient (G) at the interface and solidification rate (R). According to the study by (Moon and Metzbower, 1986), CS occurs more when G is lower, and R is higher. When it comes to the welding, as we have lower G and higher R at the center of the FZ, CS takes place more which results in dendritic growth and formation of equiaxed structure (See Fig. 11). By contrast, CS decreases from the center of the FZ toward HAZ, resulting in formation of columnar and cellular/planar structure. This explains the change in grain structure seen in this study. (Li et al., 2017) reported the same observation in their previous study for welding of NiTi to SS. It is worth noting that the transformation of equiaxed to columnar structure plays a key role in the homogeneity of properties (Kurz et al., 2001). In the case of welding, (David and Vitek, 1989) found solidification of more equiaxed structures a desirable outcome as higher homogeneity provides sufficient strength independent of loading directions. Also, Spittle (2006) believed that formation of equiaxed grains at the center of the WZ (unlike columnar structures) is beneficial in reducing the probability of centerline cracking.

On the NiTi side, the morphology of the grain structure was significantly influenced by the presence of a magnetic field during the laser welding of BM. A transformation of structure from equiaxed to columnar and then cellular can be seen for both samples from the center of FZ toward the NiTi HAZ. Comparing Fig. 4c and 4d, we can see that larger equiaxed grains with columnar structures aligned parallel to the cooling direction formed in the nMFS sample. By contrast, finer equiaxed grains and more randomly elongated columnar structures were found for the MFS sample. As discussed before, the magnetic field reduces the value of G while increases the rate of R in the pool. This promotes the CS occurrence which results in formation of finer equiaxed grains in the

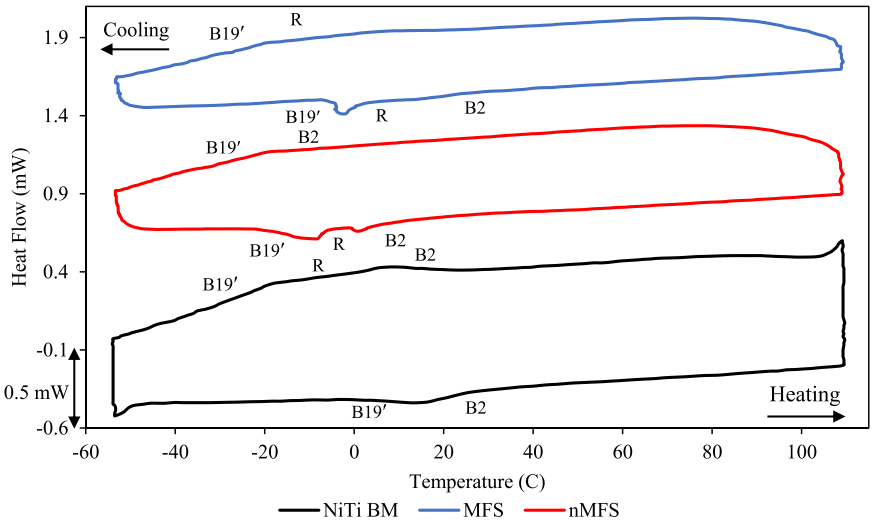

Fig. 10. DSC curves extracted from the NiTi BM, nMFS and MFS samples.

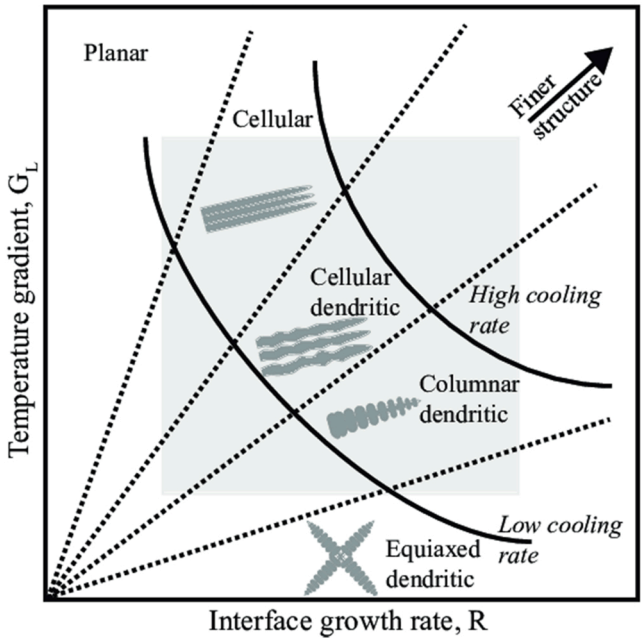

Fig. 11. Variation of interface morphology with growth rate and temperature gradient (adapted from (Agarwal, 2019)).

center of the pool. The random oriented columnar grains found in the MFS sample can also be attributed to the rotation of molten material influenced by the Lorentz force. (Li et al., 2014) investigated the effect of static magnetic field on the morphology of grains during directional solidification of six different materials, including a Nickel-base superalloy. They observed a tendency to formation of finer equiaxed grains through dendrite fragmentation under the effect of magnetic field. It was also revealed that a torque is created under the influence of Lorentz force which derives the rotation of grains, and then transformation of columnar to equiaxed occurs at a critical value of temperature gradient. This explains the formation finer equiaxed grains in higher numbers for the MFS sample. Moreover, the random orientation of columnar grains observed in this sample can be attributed to the rotations arising from the magnetic field. As explained above, Lorentz force acts on cell/dendrite boundaries and breaks them, which then leads to the rotation of grains. (Li et al., 2020b) also noticed this phenomenon in their study where growth of the columnar grains was modified due to the fracture of the dendrites occurred under the effect of the Lorentz Force. Also as discussed, with increasing the vorticity magnitude under the effect of magnetic field, the columnar structures grow in different directions. It should be noted that the change in the structure of the grains, supported by the magnetic field during laser welding, can improve the overall mechanical properties of the joint. (Frenzel et al., 2011b) observed that the formation of finer grains in the FZ prevents a reduction in the grain boundary area and thereby prevents limited transformation induced plasticity which results in superior mechanical properties, higher fracture strength, and higher functional stability. (Frenzel et al., 2011a) attributed this to the stability of finer grains which is similar to the nanocrystalline NiTi pure material. In this case a finer grain structure with more grain boundaries causes geometrical constraints and thereby delays the martensitic transformation. (Waitz and Karnthaler, 2004) showed that it will eventually reduce the irreversible effects of dislocation plasticity while the SMA alloy actuates in the predefined cyclic performance. It is also well known that formation of columnar grains can result in anisotropic properties, specifically for NiTi alloy (Farhang et al., 2020). However, as observed for the MFS sample, columnar structures elongated in different orientations can preserve the homogeneity in properties of NiTi material. This variation in texture of the grains can also affect the failure of the joint under tension. (Nematollahi et al., 2021) reported significantly higher failure strain (up to 7 %) for the NiTi alloy including randomly oriented grains compared to the ones possessing grain elongated in a specific direction. All in all, in the case of MFS welding, finer equiaxed grains and randomly oriented columnar structures formed in the FZ produced a noticeable enhancement in mechanical properties as observed in Fig. 8.

The size of the HAZ and RLZ, as another main factor providing critical information about the mode of welding and heat distribution during the process, was also extracted from the SEM results. The thickness of the HAZ and more specifically RLZ (where IMCs form majorly) regions were narrowed down in the case of MFS laser welding. The RLZ formed in the HAZ toward the NiTi side arises from the laser offset technique. (Zhang et al., 2022) reported the similar findings in their study where the RLZ composed, of a multilayered structure was observed for the offset laser welding of SS and NiTi. This is an indication of a laser welding-brazing mode in which the material on the counter beam-offset side is slightly melted. (Zhang et al., 2022) showed that the RLZ formed in this welding mode can be a potential location for precipitation of brittle IMCs. This zone is formed at the interface between the fully melted material (in this case SS) and slightly melted material (in this case NiTi) where mixing of elements predominantly occurs. Therefore, RLZ is well recognized as a multi-structured layer containing possible IMCs. (Zhang et al., 2022) used EDS analysis to investigate the composition of RLZ for the NiTi/SS offset welding. They found Fe-Ni-Ti IMCs formed at different locations of this layer, with specifically brittle phases (FeTi, Fe_2Ti) being observed. (Pouquet et al., 2012) reported formation of brittle Fe-Ti IMCs as the major issue in the welding of NiTi to SS, since it speeds up the failure of the joint under tensile loading. In this study, due to the application of a magnetic field and by considering the specific orientation of permanent magnets and movement of elements from SS toward the NiTi side, the Lorentz force acts as a brake force at the interface of the joint. The SS elements are then pushed towards the BM under the effect of Lorentz force. This limits the distribution of molten material along the wires and therefore decreases the thickness of the RLZ and HAZ observed for the MFS sample.

The change in the distribution of elements and their proportion, which affects the probability of formation of IMCs and thereby joint strength, was investigated under the effect of a magnetic field. Fe, Ni, Ti and Cr were all observed in the FZ's of both nMFS and MFS samples confirming the mixture of molten materials. However, the MFS case showed more stabilized Fe and Ni elements in the FZ. As observed from Fig. 5, lower fluctuation for two main elements (Fe and Ni) was observed in the MFS sample. (Zhang et al., 2022) proved that instability in the mixture of elements in the melt pool leads to formation of defects deteriorating the mechanical properties. Therefore, one can infer that lower fluctuation observed for the main elements of the MFS sample results in lower levels of defects and superior mechanical properties for this sample. (Zhou et al., 2021) observed a more stable element exchange for the Magnesium/Aluminum dissimilar laser welding under the effect of magnetic field. They attributed their findings to the better mixing of liquid metals and more uniform element exchange in the melt pool under the influence of magnetic field. Compared to the nMFS sample, higher atomic percentage of Fe and Cr was found in the FZ for the MFS sample with lower concentration of Ni and Ti being observed in this zone. This can be inferred as a higher contribution of SS than NiTi during the welding process under the influence of magnetic field. One can infer that more contribution from SS can preserve the NiTi characteristics which is one of the main goals of this study. (Zhang et al., 2022) observed that because of the lower solubility, Ti has severe effects on formation of potential brittle IMCs. With lower concentration of Ti observed in FZ of MFS sample, the probability of formation of Ti-contained brittle phases (such as TiFe, $TiFe_2$) is less. (Asadi et al., 2020b) found that formation of TiFe and $TiFe_2$ is the main factor in weakening the joint strength and thereby reduction of these phases avoids deteriorating the welding properties. (Tomashchuk and Sallamand, 2018) attributed the embrittlement of the Fe-Ti IMCs to the high

metallurgical incompatibility between these two elements as well as formation of residual stress. However, under the influence of a magnetic field and the Lorentz force that is directed against the fluid flow, the stirring effect is promoted which avoids moving the SS elements toward the NiTi side and keeps them in the FZ toward the SS BM. Similar observations were reported in the magnetic assisted welding studies, where circular motion of the molten material controlled distribution of the elements due to the interaction of an external current and magnetic field (Hu et al., 2022). Qi et al., also observed that such kind of motion could help in the annihilation of defects induced by the resistance spot welding in their case (Qi et al., 2021). In the current study, this interaction occurs between the external magnetic field and the current formed due to the Seebeck effect. In this case, relatively higher conductivity of SS compared to NiTi and higher Seebeck coefficient of the SS elements (Fe, Cr) in respect to the Ni and Ti form a thermoelectric current (TEC) which is proved to from the Lorentz force (Chen et al., 2018). Also, as the laser is focused on the SS side, higher temperature gradient is expected for the SS compared to NiTi, which strengthens the intensity of the current. Since there is a direct relationship between conductivity, Seebeck effect, thermal gradient and Lorentz force (Zhou et al., 2021), SS elements are affected more by this force and the effect of magnetic field. This results in shifting the FZ and melt pool toward the SS side (see Fig. 12) which confirms higher contribution of SS elements observed in EDS results. (Zhang et al., 2022) found out that more contribution of SS in this competition prevents rapid solidification of Fe in SS side and distribution of the brittle Ti-Fe compounds. However, as the aforementioned parameters vary with a change in temperature, a numerical analysis is required to model the phenomenon of the thermoelectric hydrodynamic for the melt pool that forms in MFS laser welding of SS/NiTi. It is worth noting that (Zhou et al., 2021) reported the same observation for the laser welding of Magnesium/Aluminum where formation of brittle phases was avoided by applying the magnetic field.

Formation of intermetallic phases, as a result of variation in distribution of elements and mixing effect during the welding process, is a very common phenomenon which affects the final properties of a welded joint. According to Fig. 6, regardless of parent phases associated with the BMs, the formation of FeNi, Ni_3Ti, Ti_2Ni, and $TiCr_2$ was observed for both samples, which is in agreement with the phases reported for the NiTi/SS laser welded joints (Mirshekari et al., 2013). Comparing the XRD results between nMFS and MFS samples, the peaks corresponding to the aforementioned phases were found less in number for the MFS sample. It should be noted that formation of some of these phases strengthen the joint and also improve mechanical properties. (Niu et al., 2021) showed that the presence of FeNi in the WZ greatly decreases the formation of brittle IMCs in the electron beam welding of NiTi/SS. This was reported to be due to the high solubility of Titanium in FeNi, which can result in the formation of lesser Titanium-rich IMCs (more specifically Fe-Ti phases) deteriorating the mechanical properties. They also found out that Ni3Ti phase acts as an obstacle for crack propagation in IMC regions and improves the plasticity of the joint at room temperature. Ni3Ti phase is shown to form at inter-dendritic regions close to the Fe_2Ti dendrites. (Niu et al., 2021) showed that since this phase has a certain plasticity level at ambient temperature, it is able to block the propagation of cracks forming inside the Fe_2Ti. By contrast, (Pouquet et al., 2012) reported formation of brittle Fe-Ti IMCs as a major issue in welding of NiTi/SS. With no sign of formation of these Fe-Ti IMCs, higher strength and superior mechanical properties are expected for the MFS sample. According to the results, no Fe-Ti compound was observed in the MFS sample, while both potential brittle phases (TiFe, $TiFe_2$) were detected in the nMFS sample. This can be attributed to the higher level of Ti observed in FZ of the nMFS sample (as discussed in the previous paragraph). Also as mentioned before, under the influence of magnetic field, better flow of molten material and mixing effect avoid quick solidification of Fe which prevents formation of Fe-Ti compounds.

Microhardness value, which is a good representative for the formation of IMCs and ductility of the joint, was measured for the WZ of both weldments. As shown in Fig. 7, a similar pattern for the hardness measurements was found for both nMFS and MFS samples. Both weldments showed higher hardness values for the FZ and HAZ compared to the BMs. This confirms the formation of IMCs at the WZ since it is well known that precipitation of these phases increases the hardness value (Niu et al., 2021). However, as confirmed by the XRD results, formation of brittle Fe-Ti phases in the nMFS sample resulted in higher hardness values. This is in agreement with observations from a study by (Li et al., 2017) in which formation of TiFe and $TiFe_2$ increases the hardness value

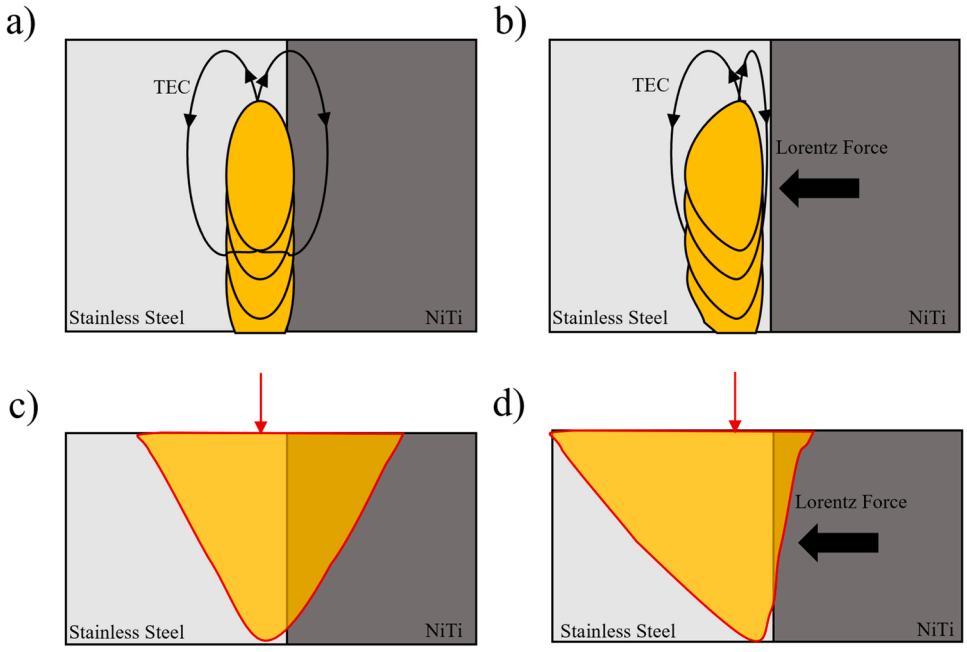

Fig. 12. Schematic of thermoelectric current (TEC) distribution and melt pool geometry in the a) nMFS and b) MFS offset laser welding from the top view. Schematic of the melt pool geometry which forms during the offset laser welding of c) nMFS and d) MFS condition from the side view. The Lorentz force pushes the thermoelectric flow and melt pool toward the SS side.

of NiTi/SS joints to around 2.2 times that of NiTi BM. Thus, higher hardness values observed at the WZ of the nMFS sample (with the maximum hardness value around 2.6 times that of NiTi BM) can be inferred as a higher level of brittleness and lower ductility at this joint. By contrast, higher ductility and superior mechanical properties are expected to be observed for the MFS sample, with the maximum hardness value at the center of the FZ being found around 1.6 times that of NiTi BM.

The ultimate strength and ductility of the connections were evaluated using uniaxial tensile tests. As shown in Fig. 8, both samples had lower ultimate tensile stress (UTS) and elongation at break compared to the BMs. (Li et al., 2013) has also reported the reduction in the strength of the laser welded NiTi-SS joints. (Vannod et al., 2011) attributed this to the rapid solidification after welding, which results in turning the metal from solid to solutionized state with no work-hardening properties. As a result, the FZ and HAZs, which experience annealing temperatures during welding process, are potential locations for the joint break, as mentioned by (Zeng et al., 2016). According to the study by (Vieira et al., 2011), dislocation removal, formation of brittle IMCs and grain size increase are some factors which weaken these zones. Additionally, (Panton et al., 2014) concluded that the reduction in ductility of the dissimilar welded superelastic SMAs is due to stress localization occurring as a result of the laser welding. Furthermore, the presence of both martensite and austenite in the weld region, and austenite in the NiTi BM, resulted in an interface between these two phases where plastic deformation has been reported to occur, which as stated by (Oliveira et al., 2016), could result in the deterioration of the mechanical properties. Nevertheless, the MFS sample showed 28 % and 137.5 % improvement in UTS and ductility compared to the nMFS sample, respectively. This can be attributed to the limited reaction layer formed in the MFS sample with no sign of precipitation of brittle Fe-Ti compounds being found in this sample. As discussed before, the magnetic field used during the laser welding process avoided the formation of Fe-Ti IMCs which led to improvements in UTS value and elongation observed for the MFS sample. It should be noted that the UTS achieved in this study for the MFS sample is significantly higher than that of regular laser welded NiTi/SS wires joints reported in the literature (150–200 MPa) (Asadi et al., 2020a). To the knowledge of the authors, the maximum UTS reported in the literature for dissimilar laser welding of NiTi/ SS is 329.5 MPa which was obtained using a large beam offset (Zhang et al., 2022). The value achieved in this study is 30 % higher which is a noticeable improvement obtained using the effect of a magnetic field.

Since the goal of this study was not only improving the strength of the NiTi/SS joint, but also preserving the characteristics of NiTi during welding, a tiny specimen of NiTi close to the FZ was selected from both samples to be analyzed and compared with the BM NiTi used in this study. As the phase transformation characteristics of shape memory alloys can be a good criterion for evaluating their functional properties (Li et al., 2020a), DSC analysis was performed on NiTi specimens selected from MFS sample, nMFS sample, and BM. As can be seen from Fig. 10, the transformation between austenitic and martensitic phases didn't occur directly, with the R phase being formed during the transformation process. (Panton et al., 2016) also observed formation of this phase in their study for the laser welded NiTi alloys, where it was attributed to the formation of precipitates during annealing before the welding process. However, for this study where no pre-treatment was used for the samples, the manufacturing method of the NiTi wires can be the causation since this phase was detected for the BM as well. Also, (Egorushkin and Kulkova, 1982) reported the formation of R phase for the NiTi alloys with relatively high Ni concentrations (like the sample used in this study). By comparing the A_f temperature extracted from the plots it can be seen that the transformation temperature of the MFS sample is similar to that of NiTi BM. Additionally a reduction in A_f was observed for the nMFS sample. This shows that the functional properties of the NiTi were preserved during the magnetic welding but changed during the regular welding process. (Hornbogen et al., 2001) observed that microstructural defects have a significant impact on transformation temperatures of NiTi alloy. This is in agreement with the findings of this study, as higher level of defects and precipitates were observed in the nMFS sample. Moreover, (Chan et al., 2012) reported a removal of cold working properties, residual stress, and grain growth during the welding process are factors leading to a reduction in transformation temperatures. Reduction in A_f observed for the nMFS sample confirms the discussion above, where a reduction in ductility of the nMFS sample was also attributed to the same factors. It is a known fact that there is an inverse relationship between Ni/Ti ratio and transformation temperatures of the NiTi alloy (Kök et al., 2016). Hence, with formation of Ti-Fe IMCs observed for the nMFS sample, and therefore depletion of Ti, an increase in Ni/Ti ratio and reduction in transformation temperatures is expected for this sample. Overall, the results extracted from DSC analysis showed that a magnetic field can preserve the phase transformation characteristics and functional properties of NiTi during laser welding. This confirms that an improvement in mechanical properties of NiTi/SS joints can be obtained by applying a magnetic field during the laser welding process, while the functionality of NiTi is also preserved.

5. Conclusions

In this study, it was hypothesized that applying a steady external magnetic field during the welding process, if set appropriately, would preserve the function ability of the NiTi while improving the strength of the joint. Comparison between the characteristics of nMFS and MFS weldments revealed the following observations:

- A deeper pool with the lower level of defects, and narrower RLZ region were formed in the MFS sample compared to the nMFS weldment.
- In terms of grain morphology, finer equiaxed grains and more randomly elongated columnar structures were observed in the MFS sample. This resulted in superior mechanical properties for this sample.
- A more stable element exchange with a higher contribution of SS than NiTi was observed under effect of the magnetic field, which this preserved the NiTi characteristics.
- By comparing the XRD results, no Fe-Ti compound was observed in the MFS sample while both potential brittle phases (TiFe, $TiFe_2$) were detected in the nMFS sample. Formation of brittle Fe-Ti phases in the nMFS sample resulted in higher hardness values for this sample.
- Based on the tensile test plots, the MFS sample showed 28 % and 137.5 % improvement in UTS and ductility compared to the nMFS sample, respectively. To the knowledge of the authors, the UTS achieved in this study is 30 % higher than the maximum UTS reported in the literature for the dissimilar laser welding of NiTi/ SS.
- By comparing the DSC plots, it was observed that the transformation temperature of the MFS sample is similar to that of NiTi BM. However, a reduction in A_f was seen for the nMFS sample. This showed that the functional properties of the NiTi were preserved during the magnetic welding but changed during the regular welding process.

6. Limitations and future avenues

This paper has investigated the effect of steady magnetic field on the laser welding of NiTi/SS wires with the improvement being achieved in mechanical properties of the joint and preservation of the thermal dependent properties of the NiTi alloy. However, the authors have identified the following limitations in this research study that may require further investigation in the future studies:

- This study only focuses on the effectiveness of the steady magnetic field on the properties of the NiTi/SS laser welded joint. However, strength of the magnetic field can also be seen as an important factor

in the MFS welding design set. Therefore, quantifying and optimizing the magnetic field should be considered in the future studies.

- As discussed in this paper, the effect of the Lorentz force on movement of the molten material can be different based on some factors including conductivity, Seebeck effect, and thermal gradient. However, since these parameters are a function of temperature, a numerical analysis is required to model the phenomenon of the thermoelectric hydrodynamic for the melt pool that forms in MFS laser welding of NiTi/SS.
- In this study, SEM results were used to discuss the morphology of the grains formed in WZ. However, the size, texture and morphology of grains should be discussed in detail using more specific microstructure analysis, like Electron Backscatter Diffraction (EBSD) technique.
- In this paper spot laser welding technique, as one of the common laser welding methods, was employed for the dissimilar joining of NiTi and SS. To comprehend the analysis of the effect of magnetic field on the dissimilar laser welding of NiTi/SS, different continuous laser welding techniques should be considered in the future studies.

CRediT authorship contribution statement

Behzad Farhang: Methodology, Formal analysis, Writing – original draft. **Ahmet Alptug Tanrikulu**: Methodology, Formal analysis, Writing – original draft. **Aditya Ganesh-Ram**: Methodology, Formal analysis, Writing – original draft. **Ankur Jain**: Conceptualization, Supervision, Writing – review & editing. **Amirhesam Amerinatanzi**: Conceptualization, Supervision, Writing – review & editing.

Declaration of Competing Interest

The authors declare that they have no known competing financial interests or personal relationships that could have appeared to influence the work reported in this paper.

Data availability

Data will be made available on request.

References

Agarwal, G., 2019. Study of solidification cracking during laser welding in advanced high strength steels: A combined experimental and numerical approach. Delft University of Technology.

Asadi, S., Saeid, T., Valanezhad, A., Watanabe, I., Khalil-Allafi, J., 2020a. The effect of annealing temperature on microstructure and mechanical properties of dissimilar laser welded superelastic NiTi to austenitic stainless steels orthodontic archwires. J. Mech. Behav. Biomed. Mater. 109, 103818.

Asadi, S., Saeid, T., Valanezhad, A., Watanabe, I., Khalil-Allafi, J., 2020b. Effects of Ni powder addition on microstructure and mechanical properties of NiTi to AISI 304 stainless steel archwire dissimilar laser welds. J. Manuf. Process. 55, 13–21.

Bhanu, V., Pandey, C., Gupta, A., 2022. Dissimilar joining of the martensitic grade P91 and Incoloy 800HT alloy for AUSC boiler application: microstructure, mechanical properties and residual stresses. CIRP J. Manuf. Sci. Technol. 38, 560–580.

Cao, L., Zhou, Q., Liu, H., Li, J., Wang, S., 2020. Mechanism investigation of the influence of the magnetic field on the molten pool behavior during laser welding of aluminum alloy. Int. J. Heat. Mass Transf. 162, 120390.

Chan, C.W., Man, H.C., Yue, T.M., 2012. Effect of postweld heat treatment on the microstructure and cyclic deformation behavior of laser-welded NiTi-shape memory wires. Metall. Mater. Trans. A 43, 1956–1965.

Chan, C.-W., Man, H.C., Yue, T., 2011. Effects of process parameters upon the shape memory and pseudo-elastic behaviors of laser-welded NiTi thin foil. Metall. Mater. Trans. A: Phys. Metall. Mater. Sci. 42, 2264–2270.

Chen, J., Wei, Y., Zhan, X., Gu, C., Zhao, X., 2018. Thermoelectric currents and thermoelectric-magnetic effects in full-penetration laser beam welding of aluminum alloy with magnetic field support. Int. J. Heat. Mass Transf. 127, 332–344.

Chen, R., 2020. Effect of external magnetic field on the microstructure and strength of laser-welded aluminum to titanium. J. Mater. Sci. 55, 4054–4064.

David, S.A., Vitek, J.M., 1989. Correlation between solidification parameters and weld microstructures. Int. Mater. Rev. 34, 213–245.

Egorushkin, V.E., Kulkova, S.E., 1982. On the theory of phase transitions in NiTi. J. Phys. F: Met. Phys. 12, 2823–2828.

Elahinia, M., 2016. Shape Memory Alloy Actuators: Design, Fabrication and Experimental. Evaluation.John Wiley & Sons.

Ellery, A., 2016. Survey of past rover missions. In: Ellery, A. (Ed.), Planetary Rovers: Robotic Exploration of the Solar System. Springer Berlin Heidelberg, Berlin, Heidelberg, pp. 59–69.

Falvo, A., Furgiuele, F.M., Maletta, C., 2005. Laser welding of a NiTi alloy: mechanical and shape memory behaviour. Mater. Sci. Eng.: A 412, 235–240.

Farhang, B., Ravichander, B.B., Venturi, F., Amerinatanzi, A., Shayesteh Moghaddam, N., 2020. Study on variations of microstructure and metallurgical properties in various heat-affected zones of SLM fabricated Nickel–Titanium alloy. Mater. Sci. Eng.: A 774, 138919.

Frenzel, J., Burow, J., Payton, E., Rezanka, S., Eggeler, G., 2011a. Improvement of NiTi shape memory actuator performance through ultra-fine grained and nanocrystalline microstructures. Adv. Eng. Mater. 13, 256–268.

Frenzel, J., Burow, J.A., Payton, E.J., Rezanka, S., Eggeler, G., 2011b. Improvement of NiTi shape memory actuator performance through ultra-fine grained and nanocrystalline microstructures. Adv. Eng. Mater. 13, 256–268.

Gugel, H., Schuermann, A., Theisen, W., 2008. Laser welding of NiTi wires. Mater. Sci. Eng.: A 481, 668–671.

Hartl, D.J., Lagoudas, D.C., 2007. Aerospace applications of shape memory alloys. Proc. Inst. Mech. Eng. Part G: J. Aerosp. Eng. 221, 535–552.

He, E., Liu, J., Lee, J., Wang, K., Politis, D.J., Chen, L., Wang, L., 2018. Effect of porosities on tensile properties of laser-welded Al-Li alloy: an experimental and modelling study. Int. J. Adv. Manuf. Technol. 95, 659–671.

Hornbogen, E., Mertinger, V., Wurzel, D., 2001. Microstructure and tensile properties of two binary NiTi-alloys. Scr. Mater. 44, 171–178.

Hu, S., Haselhuhn, A.S., Ma, Y., Li, Z., Qi, L., Li, Y., Carlson, B.E., Lin, Z., 2022. Effect of external magnetic field on resistance spot welding of aluminium to steel. Sci. Technol. Weld. Join. 27, 84–91.

Huang, L., Liu, P., Zhu, S., Hua, X., Dong, S., 2020. Experimental research on formation mechanism of porosity in magnetic field assisted laser welding of steel. J. Manuf. Process. 50, 596–602.

Kök, M., Dağdelen, F., Aydoğdu, A., Aydoğdu, Y., 2016. The change of transformation temperature on NiTi shape memory alloy by pressure and thermal ageing. J. Phys.: Conf. Ser. 667, 012011.

Kumar, A., Pandey, C., 2022a. Autogenous laser-welded dissimilar joint of ferritic/martensitic P92 steel and Inconel 617 alloy: Mechanism, microstructure, and mechanical properties. Arch. Civ. Mech. Eng. 22, 1–20.

Kumar, S., Sirohi, S., Vidyarthy, R., Gupta, A., Pandey, C., 2021. Role of the Ni-based filler composition on microstructure and mechanical behavior of the dissimilar welded joint of P22 and P91 steel. Int. J. Press. Vessels Pip. 193, 104473.

Kurz, W., Bezençon, C., Gäumann, M., 2001. Columnar to equiaxed transition in solidification processing. Sci. Technol. Adv. Mater. 2, 185–191.

Li, H., Sun, D., Cai, X., Dong, P., Gu, X., 2013. Laser welding of TiNi shape memory alloy and stainless steel using Co filler metal. Opt. Laser Technol. 45, 453–460.

Li, H.M., Sun, D.Q., Cai, X.L., Dong, P., Wang, W.Q., 2012. Laser welding of TiNi shape memory alloy and stainless steel using Ni interlayer. Mater. Des. 39, 285–293.

Li, J., Panton, B., Liang, S., Vivek, A., Daehn, G., 2020a. High strength welding of NiTi and stainless steel by impact: Process, structure and properties. Mater. Today Commun. 25, 101306.

Li, Q., Zhu, Y., Guo, J., 2017. Microstructure and mechanical properties of resistance-welded NiTi/stainless steel joints. J. Mater. Process. Technol. 249, 538–548.

Li, X., Fautrelle, Y., Gagnoud, A., Du, D., Wang, J., Ren, Z., Nguyen-Thi, H., Mangelinck-Noel, N., 2014. Effect of a weak transverse magnetic field on solidification structure during directional solidification. Acta Mater. 64, 367–381.

Li, Y.Z., Mangelinck-Noël, N., Zimmermann, G., Sturz, L., Nguyen-Thi, H., 2020b. Modification of the microstructure by rotating magnetic field during the solidification of Al-7 wt% Si alloy under microgravity. J. Alloy. Compd. 836, 155458.

Mehrpouya, M., Gisario, A., Barletta, M., Natali, S., Veniali, F., 2019. Dissimilar laser welding of NiTi wires. Lasers Manuf. Mater. Process. 6, 99–112.

Mirshekari, G.R., Saatchi, A., Kermanpur, A., Sadrnezhaad, S.K., 2013. Laser welding of NiTi shape memory alloy: comparison of the similar and dissimilar joints to AISI 304 stainless steel. Opt. Laser Technol. 54, 151–158.

Möller, F., Thomy, C., 2013. 9 - Laser welding and brazing of dissimilar materials. In: Katayama, S. (Ed.), Handbook of Laser Welding Technologies. Woodhead Publishing, pp. 255–279.

Moon, D.W., Metzbower, E.A., 1986. Temperature measurements of molten weld pool along the keyhole in laser beam welding. Welding Institute of, C. Welding for Challenging Environments. Pergamon,, pp. 41–50.

Nematollahi, M., Saghaian, S.E., Safaei, K., Bayati, P., Bassani, P., Biffi, C., Tuissi, A., Karaca, H., Elahinia, M., 2021. Building orientation-structure-property in laser powder bed fusion of NiTi shape memory alloy. J. Alloy. Compd. 873, 159791.

Niu, H., Jiang, H.C., Zhao, M.J., Rong, L.J., 2021. Effect of interlayer addition on microstructure and mechanical properties of NiTi/stainless steel joint by electron beam welding. J. Mater. Sci. Technol. 61, 16–24.

Oliveira, J.P., Fernandes, F.M.B., Schell, N., Miranda, R.M., 2016. Martensite stabilization during superelastic cycling of laser welded NiTi plates. Mater. Lett. 171, 273–276.

Panton, B., Pequegnat, A., Zhou, Y.N., 2014. Dissimilar laser joining of NiTi SMA and MP35N wires. Metall. Mater. Trans. A 45, 3533–3544.

Panton, B., Oliveira, J.P., Zeng, Z., Zhou, Y.N., Khan, M.I., 2016. Thermomechanical fatigue of post-weld heat treated NiTi shape memory alloy wires. Int. J. Fatigue 92, 1–7.

Patel, S.K., Behera, B., Swain, B., Roshan, R., Sahoo, D., Behera, A., 2020. A review on NiTi alloys for biomedical applications and their biocompatibility. Mater. Today.: Proc. 33, 5548–5551.

Pouquet, J., Miranda, R.M., Quintino, L., Williams, S., 2012. Dissimilar laser welding of NiTi to stainless steel. Int. J. Adv. Manuf. Technol. 61, 205–212.
Qi, L., Li, Z., Zhang, Q., Wu, W., Huang, N., Li, Y., 2021. Electromagnetic stirring control for resistance spot welding of SiCp/Al composites. J. Manuf. Process. 68, 1271–1279.
Quan, D., Hai, X., 2015. Shape memory alloy in various aviation field. Procedia Eng. 99, 1241–1246.
Sadashiva, M., Sheikh, M.Y., Khan, N., Kurbet, R., Gowda, T.M.D., M. Y, K., Kurbet, R, N., Gowda, T.M.D., 2021. A Review on Application of Shape Memory Alloys. Int. J. Recent Technol. Eng. 9, 111–120.
Shamsolhodaei, A., Oliveira, J.P., Schell, N., Maawad, E., Panton, B., Zhou, Y.N., 2020. Controlling intermetallic compounds formation during laser welding of NiTi to 316L stainless steel. Intermetallics 116, 106656.
Spittle, J.A., 2006. Columnar to equiaxed grain transition in as solidified alloys. Int. Mater. Rev. 51, 247–269.
Tomashchuk, I., Sallamand, P., 2018. Metallurgical strategies for the joining of titanium alloys with steels. Adv. Eng. Mater. 20, 1700764.
Vannod, J., Bornert, M., Bidaux, J.E., Bataillard, L., Karimi, A., Drezet, J.M., Rappaz, M., Hessler-Wyser, A., 2011. Mechanical and microstructural integrity of nickel–titanium and stainless steel laser joined wires. Acta Mater. 59, 6538–6546.
Vieira, L.A., Fernandes, F.M.B., Miranda, R.M., Silva, R.J.C., Quintino, L., Cuesta, A., Ocaña, J.L., 2011. Mechanical behaviour of Nd:YAG laser welded superelastic NiTi. Mater. Sci. Eng.: A 528, 5560–5565.
Vollertsen, F., Thomy, C., 2006. Magnetic stirring during laser welding of aluminum. J. Laser Appl. 18, 28–34.
Waitz, T., Karnthaler, H.P., 2004. Martensitic transformation of NiTi nanocrystals embedded in an amorphous matrix. Acta Mater. 52, 5461–5469.
Zeng, Z., Oliveira, J.P., Yang, M., Song, D., Peng, B., 2017. Functional fatigue behavior of NiTi-Cu dissimilar laser welds. Materials & Design 114, 282–287.
Zeng, Z., Yang, M., Oliveira, J.P., Song, D., Peng, B., 2016. Laser welding of NiTi shape memory alloy wires and tubes for multi-functional design applications. Smart Mater. Struct. 25, 085001.
Zhang, K., Peng, P., Zhou, Y.N., 2022. Laser welding-brazing of NiTi/304 stainless steel wires with beam defocus and large offset. Mater. Sci. Eng.: A 835, 142660.
Zhang, Y., Zeng, H., Zhou, J., Xue, R., Sun, D., Li, H., 2020. Characterization of laser beam offset welding TiNi alloy and 304 stainless steel with different joining modes. Opt. Laser Technol. 131, 106372.
Zhou, J., Zhou, D., Liu, J., 2021. Numerical and experimental investigation of magnesium/aluminum laser welding with magnetic field. The International Journal of Advanced Manufacturing Technology 116 (1–2), 545–559.
DellaCorte, C., 2017. Ni-Ti Alloys for Aerospace Bearing Applications. In World Tribology Congress (WTC 2017) (No. GRC-E-DAA-TN42521).